Characterization of Steel Rebar Spacing using Synthetic Aperture Radar Imaging

Jie Hu, Qixiang Tang, Jones Owusu Twumasi and Tzuyang Yu
Department of Civil and Environmental Engineering
University of Massachusetts Lowell
One University Avenue, Lowell, MA 01854, U.S.A.

ABSTRACT

Steel rebars is a vital component in reinforced concrete (RC) and prestressed concrete structures since they provide mechanical functions to those structures. Damages occurred to steel rebars can lead to the premature failure of concrete structures. Characterization of steel rebars using nondestructive evaluation (NDE) offers engineers and decision makers important information for effective/good repair of aging concrete structures. Among existing NDE techniques, microwave/radar NDE has been proven to be a promising technique for surface and subsurface sensing of concrete structures. The objective of this paper is to use microwave/radar NDE to characterize steel rebar grids in free space, as a basis for the subsurface sensing of steel rebars inside RC structures. A portable 10-GHz radar system based on synthetic aperture radar (SAR) imaging was used in this paper. Effect of rebar grid spacing was considered and used to define subsurface steel rebar grids. Five rebar grid spacings were used; 12.7 cm (5 in.), 17.78 cm (7 in.), 22.86 cm (9 in.), 27.94 cm (11 in.), and 33.02 cm (13 in.) # 3 rebars were used in all grid specimens. All SAR images were collected inside an anechoic chamber. It was found that SAR images can successfully capture the change of rebar grid spacing and used for quantifying the spacing of rebar grids. Empirical models were proposed to estimate actual rebar spacing and contour area using SAR images.

Keywords: Steel rebar, synthetic aperture radar, rebar spacing, NDE

1. INTRODUCTION

Reinforced concrete is a widely used construction material in many countries. Steel rebars play an important role in reinforced concrete (RC) and prestressed concrete structures since they provide tensile strength, toughness and ductility to those structures. Deterioration or damage of RC is mainly due to the corrosion of steel rebars inside the concrete structures, resulting in the premature failure of concrete structures. Characterization of steel rebars in concrete structures is important as it can provide civil engineers useful information for structural repair and rehabilitation.[1] Usually, such characterization should be performed without causing damage. Therefore, nondestructive evaluation (NDE) methods are used for the evaluation of RC structures.

There are many NDE methods applied to RC structures, including acoustic emission, thermo-infrared, optical, microwave/radar, etc. Among existing NDE methods, microwave/radar NDE has been proven to be a promising method for surface and subsurface sensing of RC structures. Li conducted experiment research using acoustic emission on a RC specimen to detect and monitor steel rebar corrosion.[2] They found that acoustic emission can detect steel rebar corrosion earlier than half-cell potential measurements or galvanic current. Weng reported the use of acoustic emission for detecting steel rebar corrosion of RC bridges.[3] Beak integrated electromagnetic heat induction and infrared thermography for detecting steel rebar corrosion.[4] By taking the advantage of thermal property of corroded and non-corroded steel rebars, they found a relationship between the IR thermal characteristics and the corrosion level of steel rebars. In view of the limitations of infrared thermography (affected by temperature), Clark used infrared thermography techniques, which was possible to detect small temperature change in corroded rebars.[5] Their methods successfully identified the internal corrosion of concrete bridges. In terms of using thermal infrared techniques, Hassan reported the use of optical based sensors for monitoring

Further author information: (Send correspondence to T. Yu)
E-mail: tzuyang_yu@UML.EDU, Telephone: 1 978 934 2288

corroded steel rebars through etched cladding bragg grating.[6] They reported that optical fiber sensor may be able to locate the position of corrosion. Lee designed a sensor using a sacrificial plate identical to a target structure was monitored by the fiber bragg gratings.[7] Szymanik combined the microwave excitation techniques with active infrared thermography.[8] Instead of acoustic emission, thermo-infrared or optical techniques, ground penetrating radar (GPR) was used for nondestructive testing of concrete structures.[9,10] They demonstrated that the application of GPR was suitable for detecting rebars, voids and detachments. To our best knowledge, no reported work on the use of synthetic aperture radar (SAR) for detecting of rebars and rebar spacing.

The objective of this research is to investigate steel rebar spacing by using a SAR imaging system. In this paper, the SAR algorithm is presented first, followed by the introduction of a SAR system. A rebar frame that is fabricated at five rebar spacings (12.7 cm (5 in.), 17.78 cm (7 in.), 22.86 cm (9 in.), 27.94 cm (11 in.), and 33.02 cm (13 in.)) are studied. The experimental results are discussed with major findings summarized.

2. THEORETICAL BACKGROUND

In SAR imaging, sripmap, spotlight and inverse modes are frequently used. For stripmap mode, it is typically used in scanning large areas. For spotlight and inverse modes, they are used in generating the highest resolution SAR images. In this research work, stripmap SAR imaging was selected.

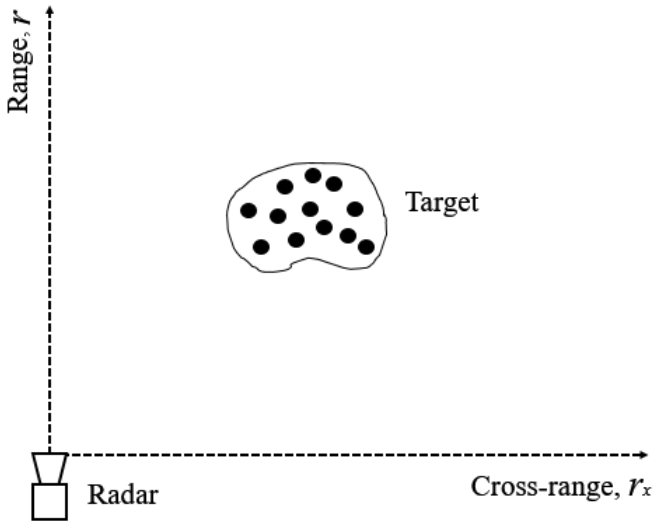

Figure 1: Stripmap of SAR imaging

In stripmap SAR imaging mode, range (r) represents the forward-looking direction of a radar. While the cross-range (r_x) represents the direction perpendicular to the range direction. Schematic configuration of stripmap SAR imaging is illustrated in Figure 1. For SAR imaging sensing, it is based on backprojection algorithm. As shown in Figure 1, at each location of imaging radar, the incident wave with an unit amplitude is defined as[11]

$$\psi_{inc}(\bar{r}) = \frac{1}{r} \cdot \exp i\bar{k_i} \cdot \bar{r} \tag{1}$$

where $\bar{k_i} = k_{ix}\hat{x} - k_{iy}\hat{y}$ = the incident wave vector, $\bar{r}$ = the relative position from the radar to any observation position, i = imaginary number. Both $\hat{x}$ and $\hat{y}$ are unit vectors in a Cartesian coordinate system. The configuration of scattered wave and configuration of incident are illustrated in Figure 2. The scattered wave from scatter j at $\bar{r_j}$ but observed at $\bar{r}$ is given in Eq.(2):

$$\psi_{scat}(\bar{r}, \bar{r_j}) = \frac{s_j(\bar{r}, \hat{k_i})}{|\bar{r} - \bar{r_j}|} \cdot \exp(ik|\bar{r} - \bar{r_j}|) \cdot \psi_{inc}(\bar{r}) \tag{2}$$

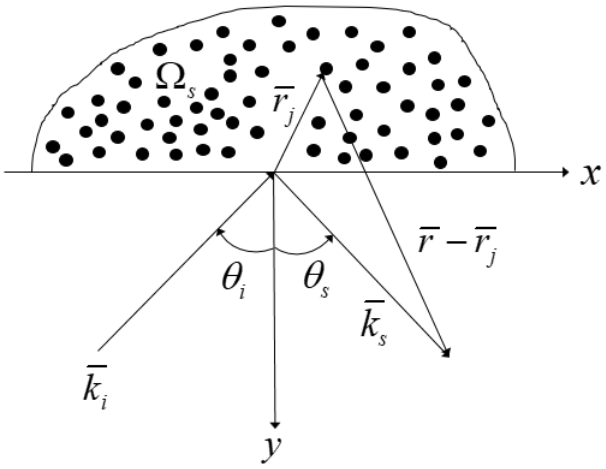

Figure 2: Scattering of N points scatters

where $s_j = s_j(\bar{r}, \hat{k_i})$ = the scattered amplitude at scatter j due to an incident wave at $\hat{k_i}$ observed at $\bar{r}$. When the interaction between scatters is neglected, the total scattered field from N scatters but observed at $\bar{r}$ is summed as the scattered fields from all scatters. According to two-dimensional Fourier transform (FT), a sliced projection in domain Ω_s is described as:

$$\psi_{scat}(\bar{r}) = \sum_{j=1}^{N} \frac{s_j(\bar{r}, \hat{k_i})}{|\bar{r} - \bar{r_j}|} \cdot \exp(ik|\bar{r} - \bar{r_j}|) \cdot \psi_{inc}(\bar{r}) \tag{3}$$

where $\bar{k_s} = k_{sx}\hat{x} + k_{sy}\hat{y}$ = the scattered wave vector, $\bar{k_i} = -\bar{k_i}$ happens when radar works as a monostaic mode. Since $k = \omega/c$ and $\theta = \theta_i = \tan^{-1}(k_{iy}/k_{ix})$, the Eq.(2) can be rewritten as:

$$\psi_{scat}(\omega, \theta) = \psi_{scat}(r, \bar{r_s}) = \frac{s_\theta}{r^2} \cdot \exp\left[\frac{r}{c}\omega(1 + \cos^2\theta - \sin^2\theta)\right] \tag{4}$$

The one-dimensional (1D) inverse FT (IFT) is used to produce sub-images in backprojection algorithm. But the final image is generated through the summation of all sub-images. The scattering response in sub-images is expressed in the following equation:

$$P(\upsilon, \theta) = \int_{\omega_{min}}^{\omega_{max}} d\omega(\omega - \omega_c, \theta)|\omega - \omega_c| \cdot \exp(-i\omega\upsilon) \tag{5}$$

$$= \frac{s_\theta}{r^2} \cdot \int_{\omega_{min}}^{\omega_{max}} d\omega|\omega - \omega_c| \cdot \exp\left[i\frac{r}{c}(\omega - \omega_c)(1 + \cos^2\theta - \sin^2\theta) - i\omega\upsilon\right] \tag{6}$$

where υ= spatial variable of 1D IFT projection. When transforming the local 1D IFT coordinate $(\upsilon, P(\upsilon, \theta))$ to global polar coordinate (r, ϕ), υ is written in the following form.

$$\upsilon = r\cos(\phi - \theta_s) \tag{7}$$

To improve image quality, the transformation from $P(\upsilon, \theta)$ to $P(r\cos(\phi - \theta))$ is required, which is associated with upsampling. Thus, the final backprojection image is the integral of sub-images along the entire synthetic aperture:

$$I(r, \phi) = \int_{-\theta_{int}/2}^{\theta_{int}/2} d\theta \cdot P(r\cos(\phi - \theta_s), \theta) \tag{8}$$

Therefore, the final version of backprojection SAR image amplitude $I(r, r_x)$ in range-cross-range plane is expressed in the following

$$I(r, r_x) = \int_{-\infty}^{\infty} h\left(t - \frac{2r'}{c}\right) \exp^{-4i\pi\frac{r'}{\lambda}} \cdot A(r') \int_0^{R_x} S(r', r'_x) \cdot a\left(\frac{r_x - r'_x}{R_0}\right) \exp^{-iF(r_x - r'_x)^2} dr'_x dr' \tag{9}$$

where h = a matched filter, t = time, c = the velocity of light, λ = wavelength, A = a function accounting for antenna pattern, processing gain and the range spreading loss, R_x = maximum cross-range, S = scattering amplitude, a = the two-way amplitude azimuth antenna pattern, R_0 = range location of the radar and F = a focusing function.

3. EXPERIMENTATION

3.1 Specimen preparation

Purchased long steel rebars were cut into small pieces at a length of 15 in. Surface rust on the steel rebar was first cleaned by a steel brush. Figure 3 shows the rebars used in our experiment.

Figure 3: Rebars preparation for the experiment

3.2 Instrument introduction

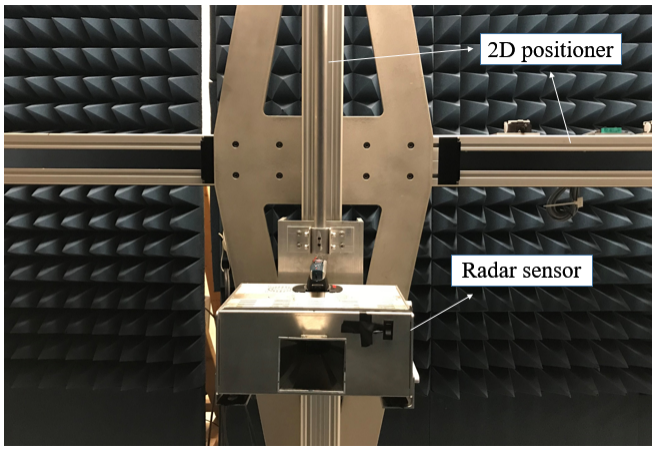

Figure 4: Imaging radar system

The imaging radar system consists of three parts: a radar sensor, a positioner and a desktop personal computer. The radar sensor has a signal generator, a radar antenna and a power supply. With the help of a biaxial positioner, the radar can move both in vertical and horizontal directions at a given step increment. The frequency range and the bandwidth of the radar system are 8-18 GHz and 4 GHz, respectively. Figure 4 shows the imaging radar system.

3.3 Experimental procedure

In this experiment, the range and cross-range of the SAR were set to be 60 cm and 80 cm, respectively. A single rebar was investigated first. The rebar was placed in front of the radar sensor. To avoid noise effect, SAR images were collected inside an anechoic chamber. Figure 5 shows the experiment setup of single steel rebar.

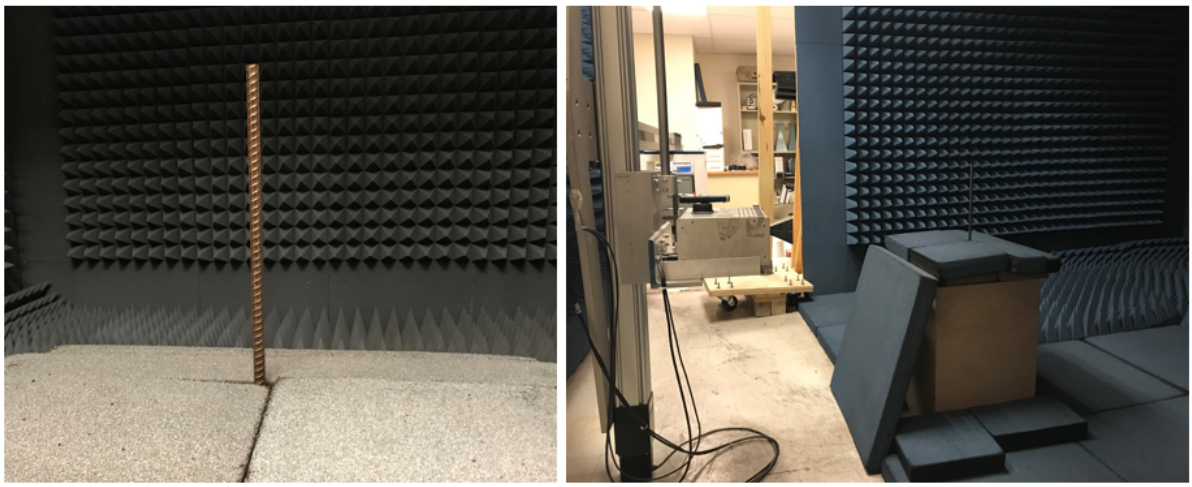

Figure 5: Single steel rebar setup: (a) single rebar located in front of radar, (b) the experiment setup

To explore the rebar spacing effect, a rebar frame was fabricated. This rebar frame was bonded by a cotton string, whose dielectric constant was approximate to 1 (aviod noise effect).[12] The rebar spacing of the frame was adjustable. Five rebar spacings (12.7 cm (5 in.), 17.78 cm (7 in.), 22.86 cm (9 in.), 27.94 cm (11 in.), and 33.02 cm (13 in.)) were considered in our experiment.

4. RESULTS AND FINDINGS

4.1 Single rebar investigation

Before investigating the effect of steel rebar spacing on SAR images, the pattern of single rebar SAR images was first studied. Figure 6 shows the configuration and its corresponding SAR image at 60-cm range. In Figure 6, a strong scatterer centered at range = 60 cm and cross-range = 40 cm was reconstructed by the SAR imaging algorithm. This strong scatterer indicated the integrated specular return of a steel rebar at range 60 cm. The shape (distribution of SAR amplitudes) of the scatterer was related to rebar geometry. Adjacent to the strong scatterer, few ring-shape secondary scatterers were also reconstructed, representing multiple reflections between the steel rebar and the radar antenna. Local maximum SAR amplitudes on each cross-range were indicated by a curve in Figure 6 (b). Furthermore, it was observed that the local maximum SAR amplitudes near the center of strong scatterer are less fluctuating. This is due to the geometric scattering effect of a round-shape cylinder (steel rebar). Average range of local maximum SAR amplitudes was calculated by

$$r_{avg} = \frac{\Sigma_{i=1}^{n} r_i}{n} \tag{10}$$

where r_i = the range value of local maximum SAR amplitude at cross-range i, and n = total number of local maximum SAR amplitudes. In this case, the average range of Figure 6 (b) was 60.625 cm with a 1.04% error.

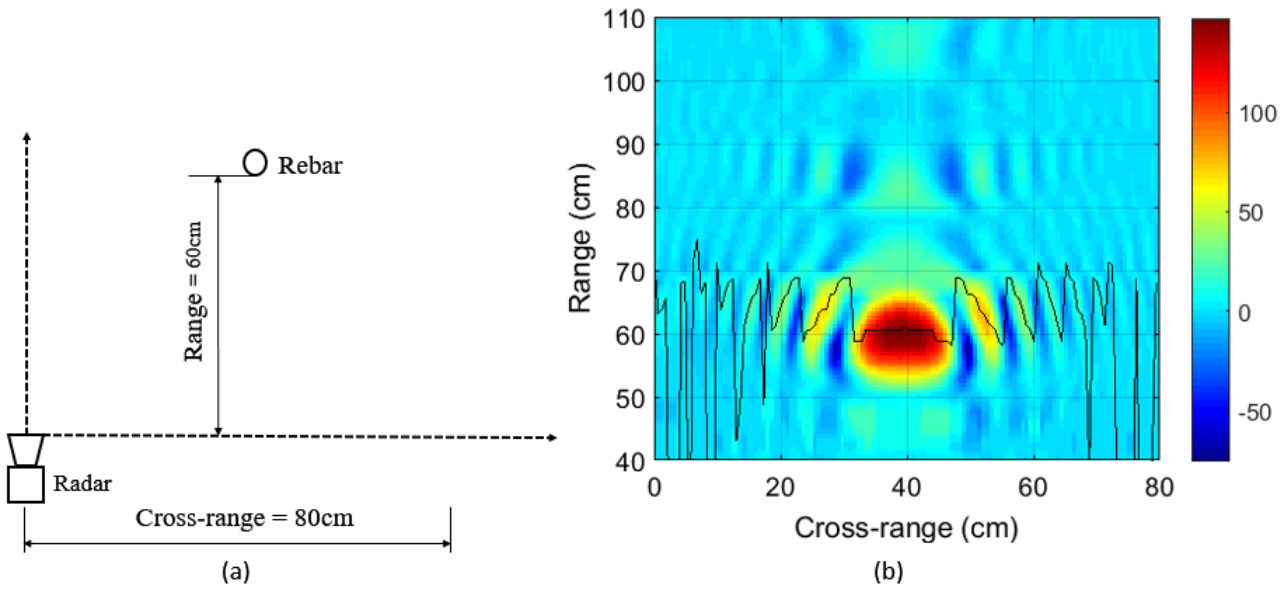

Figure 6: (a) Schematic configuration of a single rebar, (b) single rebar SAR image

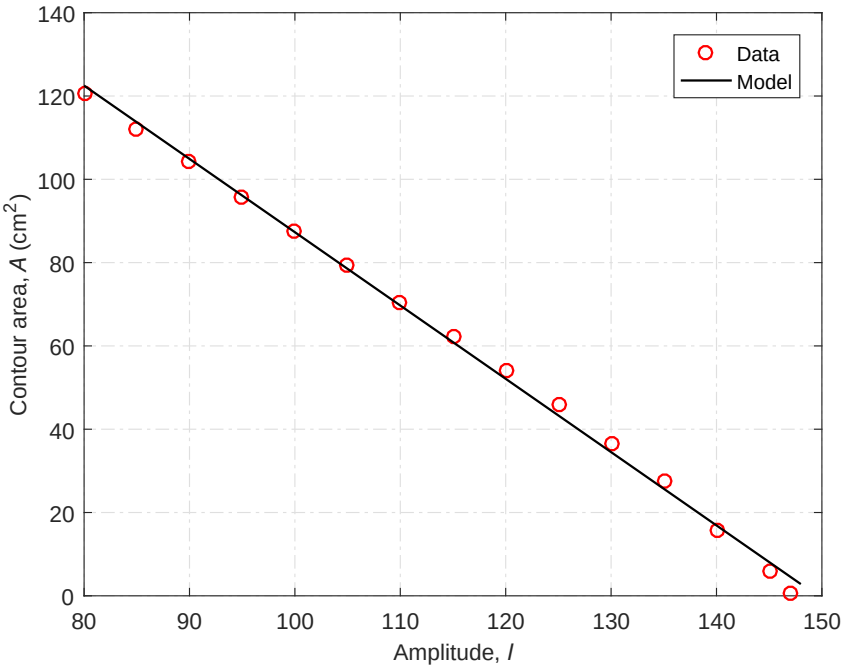

Figure 7: Contour areas vs. amplitude

The strong scatterer in Figure 6 (b) was also analyzed by studying the pattern of SAR amplitude distribution or contours at various SAR amplitudes. It was observed that the contour area of SAR amplitudes decreases with the increase of SAR amplitudes. An empirical model was developed as follows.

$$A(I) = 263.3 - 1.76I \tag{11}$$

where $A(I)$ = contour area (cm^2), and I = SAR amplitude. The coefficient of determination of Eq.(11) was 0.997. Figure 7 illustrates the performance of Eq.(11). The contour area at different amplitudes is given in Table 1.

Table 1: Contour area at different amplitudes

Amplitude, I	Contour area, A (cm^2)
80	120
85	112.2
90	104.1
95	95.9
100	87.6
105	79.2
110	70.6
115	62.2
120	54.0
125	45.8
130	36.7
135	27.4
140	15.9
145	5.7
147	0.5

4.2 Rebar spacing investigation

In the study of steel rebar spacing, an apparatus made of two steel rebars was used, as shown in Figure 8 (a). The center-to-center distance between two steel rebars was quantified by rebar spacing denoted by d. SAR images of the two rebar apparatus at five rebar spacings were collected, as shown in Figure 8 (b) to (f). In Figure 8

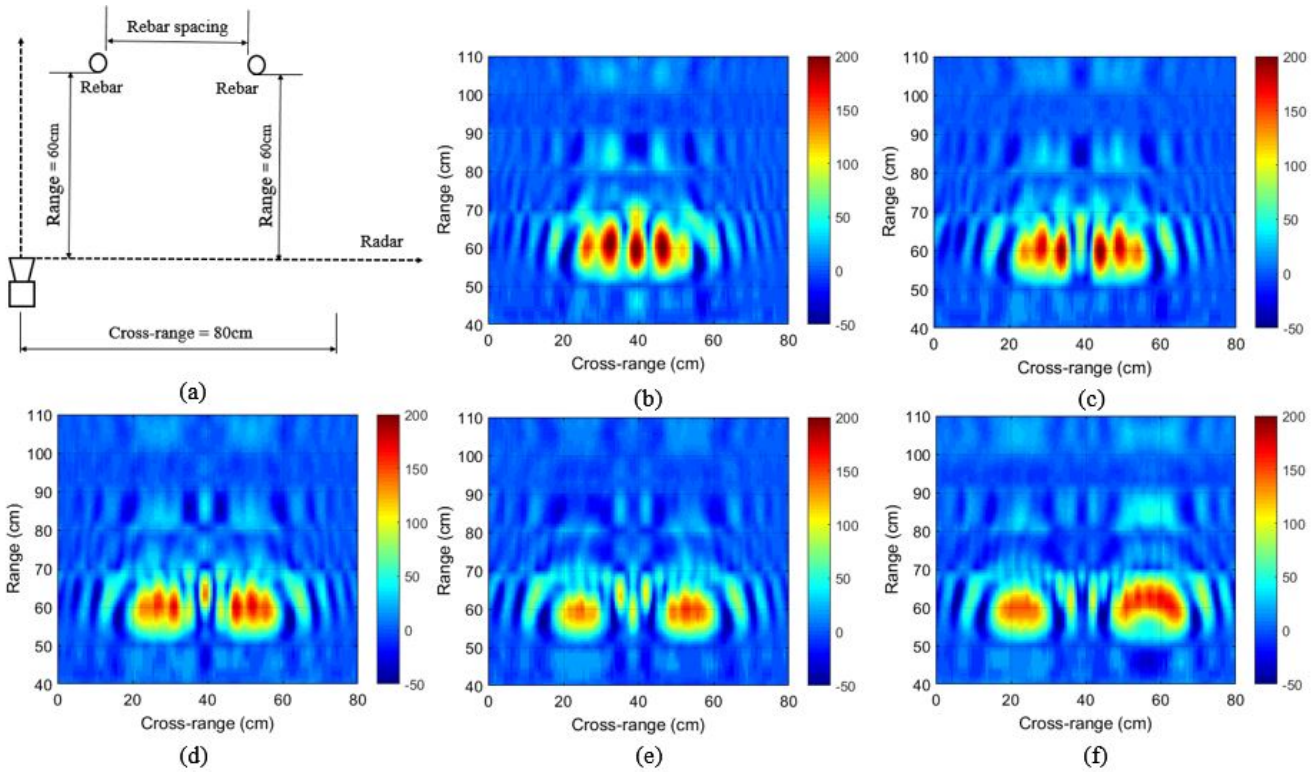

Figure 8: SAR images at different rebar spacing: (a) Schematic configuration of two rebars (b) $d_1 = 12.7$ cm (5 in.), (c) $d_2 = 17.28$ cm (7 in.), (d) $d_3 = 22.86$ cm (9 in.), (e) $d_4 = 27.94$ cm (11 in.), (f) $d_5 = 33.02$ cm (13 in.)

(b) to (f), similar pattern of scatterers was found with enhanced ring-shape secondary scatterers representing multiple reflections from i) between steel rebar and radar antenna (rebar-antenna reflection), and ii) between steel

rebars (rebar-rebar reflection). Also in Figure 8 (b) to (f), it was found that secondary scatterers representing rebar-antenna reflections basically maintains their pattern at various rebar spacings. Other secondary scatterers representing rebar-rebar reflections were amplified by the decrease of rebar spacing as expected.

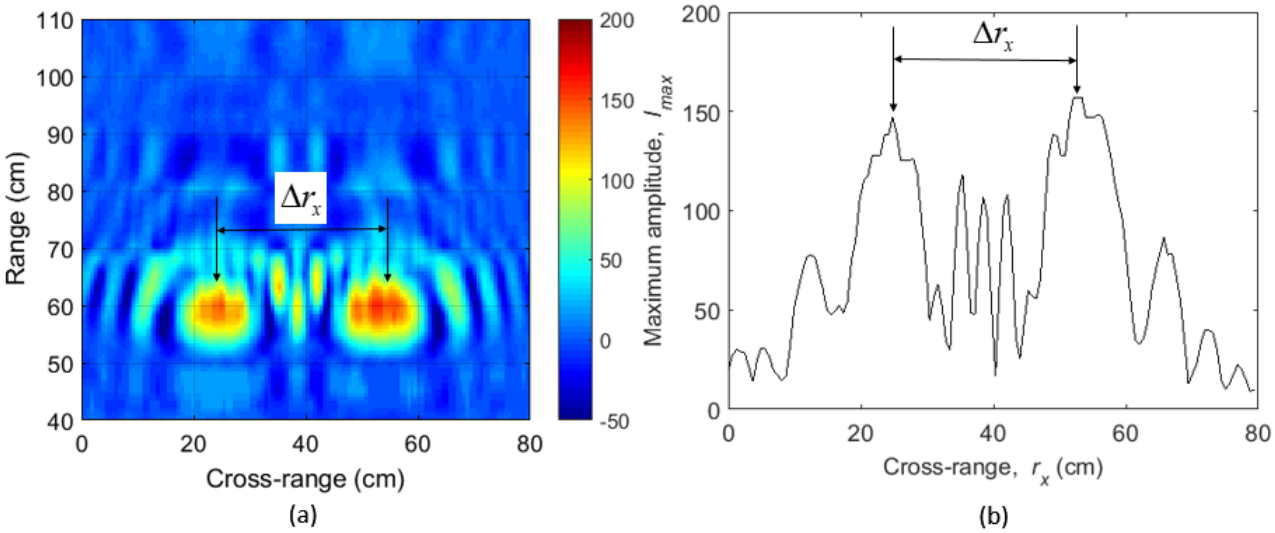

Figure 9: (a) SAR image at rebar spacing $d_4 = 27.94$ cm (11 in). (b) definition of cross-range coordinate difference Δr_x at $d_4 = 27.94$ cm (11 in.)

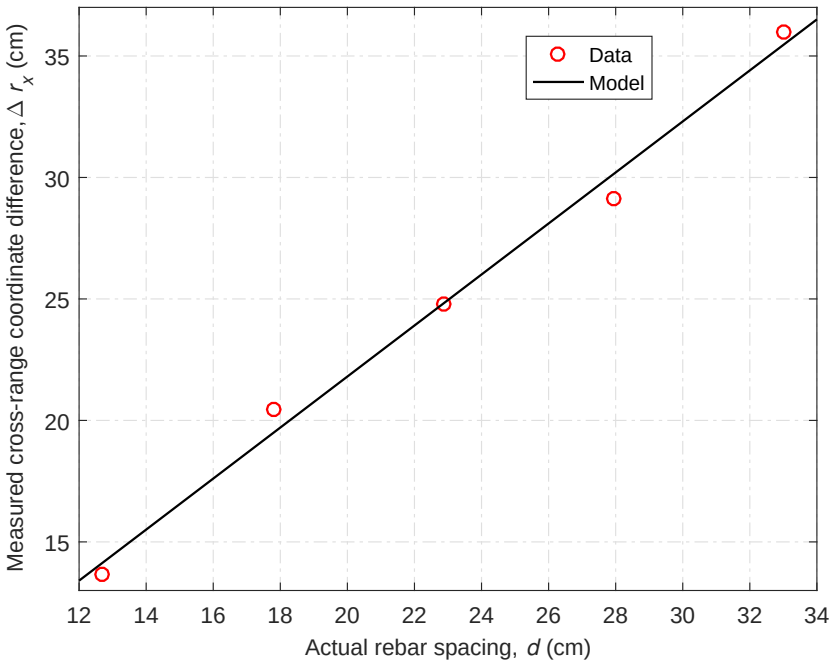

Figure 10: Actual rebar spacing vs. measured cross-range coordinate difference

In order to use SAR images for estimating steel rebar spacing in this research, cross-range coordinate difference Δr_x was defined and used. Cross-range coordinate difference Δr_x was defined by the distance between two local maximum SAR amplitudes on the cross-range axis. In Figure 9 (a), the SAR image of 27.94 cm (11 in.) rebar

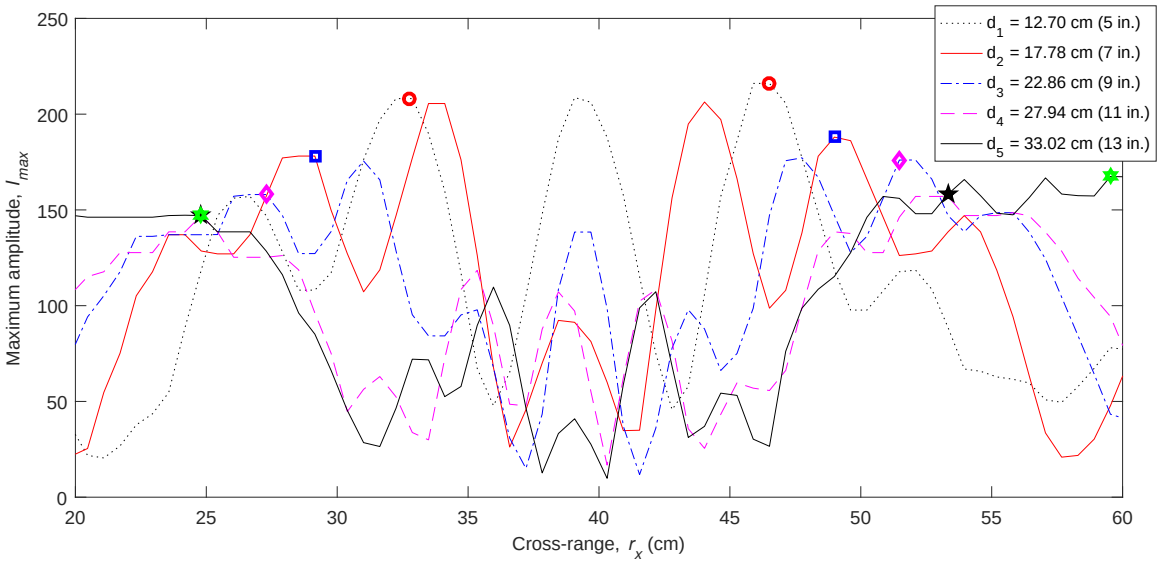

Figure 11: Maximum amplitude vs. actual rebar spacing

spacing is shown. Extracted from Figure 9 (b), a SAR curve at 60 cm range is provided. In Figure 9 (b), cross-range coordinate difference Δr_x is calculated by finding the distance between two local maximum SAR amplitudes. Figure 11 illustrates the maximum amplitude at difference rebar spacings. The highlighted points in Figure 11 are used to calculate the cross-range coordinates.

The cross-range coordinate difference values of all SAR images at five rebar spacings were determined as shown in Figure 10. A linear empirical model was developed for relating cross-range coordinate difference Δr_x to steel rebar spacing d, also shown in Figure 10. Eq. (12) provides the expression of this empirical model.

$$\Delta r_x(d) = 1.05d + 0.806 \tag{12}$$

where d = determined rebar spacing (cm), Δr_x = cross-range coordinate difference (cm) and the coefficient of determination of Eq.(12) was 0.99. To use information from SAR images for estimating actual steel rebar spacing, Eq. (12) was re-arranged into Eq. (13).

$$d(\Delta r_x) = 0.95\Delta r_x - 0.77 \tag{13}$$

Eq. (13) represents the empirical model for estimating actual steel rebar spacing d by using cross-range coordinate difference Δr_x from SAR images.

Table 2: Actual rebar spacing, measured cross-range coordinate difference and their corresponding error

Actual rebar spacing (cm)	Measured cross-range coordinate difference (cm)	Error (%)
$d_1 = 12.70$	13.63	7.40
$d_2 = 17.78$	20.47	15.07
$d_3 = 22.86$	24.05	8.49
$d_4 = 27.94$	29.76	4.29
$d_5 = 33.02$	35.94	8.90

5. CONCLUSION

This paper reports our experimental study on the SAR images of single rebar specimen and two-rebar specimen with various rebar spacings (12.7 cm (5 in.), 17.78 cm (7 in.), 22.86 cm (9 in.), 27.94 cm (11 in.), and 33.02 cm (13 in.)). In the single rebar imaging result, it is found that contour area linearly decreases with the increase of SAR amplitude. In the two-rebar imaging result, the rebar-antenna reflection is not affected by the change of rebar spacing in the SAR images of the two-rebar specimen. On the other hand, the rebar-rebar reflection is enhanced by the decrease of rebar spacing. The center-to-center distance in SAR images of two-rebar specimen can be used to predict actual rebar spacing. An empirical model is proposed to estimate actual steel rebar spacing, using SAR imaging.

6. ACKNOWLEDGMENT

The authors thank Mr. Gary Howe, Director of Laboratories, in the Department of Civil and Environmental Engineering at the University of Massachusetts Lowell for his help on specimen preparation.

REFERENCES

[1] Hu, J. and Yu, T., "Enhanced pvdf properties by multi-wall carbon nanotubes (mwcnt) for efficient energy harvesting," in [Sensors and Smart Structures Technologies for Civil, Mechanical, and Aerospace Systems 2017], 10168, 101680F, International Society for Optics and Photonics (2017).

[2] Zdunek, A. D., Prine, D., Li, Z., Landis, E., Shah, S., et al., "Early detection of steel rebar corrosion by acoustic emission monitoring," (16) (1995).

[3] Weng, M. S., Dunn, S. E., Hartt, W. H., and Brown, R. P., "Application of acoustic emission to detection of reinforcing steel corrosion in concrete," Corrosion 38(1), 9–14 (1982).

[4] Baek, S., Xue, W., Feng, M. Q., and Kwon, S., "Nondestructive corrosion detection in rc through integrated heat induction and ir thermography," Journal of Nondestructive Evaluation 31(2), 181–190 (2012).

[5] Sokavcic, A., Application of infrared thermography to the non-destructive testing of concrete structures, PhD thesis, Gradjevinski fakultet, Sveuvcilivste u Zagrebu (2010).

[6] Hassan, M. R. A., Bakar, M. H. A., Dambul, K., and Adikan, F. R. M., "Optical-based sensors for monitoring corrosion of reinforcement rebar via an etched cladding bragg grating," Sensors 12(11), 15820–15826 (2012).

[7] Lee, J.-R., Yun, C.-Y., and Yoon, D.-J., "A structural corrosion-monitoring sensor based on a pair of prestrained fiber bragg gratings," Measurement Science and Technology 21(1), 017002 (2009).

[8] Szymanik, B., Frankowski, P. K., Chady, T., and John Chelliah, C. R. A., "Detection and inspection of steel bars in reinforced concrete structures using active infrared thermography with microwave excitation and eddy current sensors," Sensors 16(2), 234 (2016).

[9] Maierhofer, C., "Nondestructive evaluation of concrete infrastructure with ground penetrating radar," Journal of Materials in Civil Engineering 15(3), 287–297 (2003).

[10] Hu, J. and Tao, J., "Energy harvesting from pavement via pvdf: Hybrid piezo-pyroelectric effects," in [Geo-Chicago 2016], 556–566 (2016).

[11] Kak, A. C. and Slaney, M., "Principles of computerized tomographic imaging," (1988).

[12] Mustata, F. S. C. and Mustata, A., "Dielectric behaviour of some woven fabrics on the basis of natural cellulosic fibers," Advances in Materials Science and Engineering 2014 (2014).